Supercritical adsorption in micro- and meso-porous carbons and its utilisation for textural characterisation

Humera Ansari [a], Lisa Joss [b], Junyoung Hwang [a], J.P. Martin Trusler [a], Geoffrey Maitland [a], Ronny Pini [a,*]

[a] *Department of Chemical Engineering, Imperial College London, London, SW7 2AZ, UK*
[b] *Department of Chemical Engineering & Analytical Science, The University of Manchester, Manchester, M13 9PL, UK*

A R T I C L E   I N F O

A B S T R A C T

Understanding supercritical gas adsorption in porous carbons requires consistency between experimental measurements at representative conditions and theoretical adsorption models that correctly account for the solid's textural properties. We have measured unary CO_2 and CH_4 adsorption isotherms on a commercial mesoporous carbon up to 25 MPa at 40 °C, 60 °C and 80 °C. The experimental data are successfully described using a model based on the lattice Density Functional Theory (DFT) that has been newly developed for cylindrical pores and used alongside Ar (87K) physisorption to extract the representative pore sizes of the adsorbent. The agreement between model and experiments also includes important thermodynamic parameters, such as Henry constants and the isosteric heat of adsorption. The general applicability of our integrated workflow is validated by extending the analysis to a comprehensive literature data set on a microporous activated carbon. This comparison reveals the distinct pore-filling behaviour in micro- and mesopores at supercritical conditions, and highlights the limitations associated with using slit-pore models for the characterisation of porous carbons with significant amounts of mesoporosity. The lattice DFT represents a departure from simple adsorption models, such as the Langmuir equation, which cannot capture pore size dependent adsorption behaviour, and a practical alternative to molecular simulations, which are computationally expensive to implement.

1. Introduction

The adsorption of supercritical gases on porous carbon materials is relevant to many industrial processes. Activated carbons continue to be widely employed for high-pressure gas separations [1] and gas storage applications by adsorption technology [2,3]. Porous carbonaceous structures are also found in natural environments, where they form the organic matter of sedimentary rocks, such as shale and coal seams [4]. Because the extraction of natural gas (mostly methane, CH_4) from these deep geologic formations relies largely on its desorption from the rock's matrix, the recovery can be enhanced through an in situ adsorption/desorption process triggered by the injection of supercritical carbon dioxide (CO_2) [5,6]. Consistency between experimental adsorption measurements at representative conditions and theoretical adsorption models is key to the design and optimisation of these adsorption-based processes [7,8]. However, the prediction of supercritical adsorption on porous carbons remains a challenging task, requiring knowledge (and use) of the adsorbent's textural parameters (e.g., geometry and size of the pores), in addition to the accurate

description of the physical behaviour of gases under confinement [9–11]. This becomes particularly important for materials that contain large amounts of mesoporosity, which can improve the adsorbent's performance at high pressures, in terms of both capacity and selectivity [12]. However, the use of supercritical data to model adsorption processes is partly hampered by the lack of an unambiguous definition of the volume of the adsorbed phase in mesoporous materials [13].

The adsorptive characteristics that qualify the porous carbon material for its intended application depend largely on its textural properties. Activated carbons (AC) draw their versatility from a broad pore-size distribution, including large amounts of micro- (pore width <2 nm), meso- (2–50 nm) and macro-porosity (>50 nm) [14]. At one end of this spectrum are natural carbonaceous materials (i.e. coal and organic-rich shale), where the environmental "activation" process has resulted into an even larger variation of pore sizes, from subnano- to micro-metres [4]. At the other end of the spectrum are synthetic porous carbons with an ordered pore-structure. These include (i) carbon molecular sieves (CMS), which can be produced with a very narrow distribution of micropores that enables exploiting them for kinetic

---

* Corresponding author.
  E-mail address: r.pini@imperial.ac.uk (R. Pini).

separations [15]; and (ii) mesoporous carbons (MC) that possess a highly-uniform periodic mesoporous structure with well-defined cylindrical pores [16]. Because they can be considered as the building blocks of more complex porous structures, ordered carbons are important reference materials for the textural characterisation of industrial adsorbents by physisorption [17] and for the development of advanced models that describe the phase behaviour of fluids in pores [18]. In this context, a major distinction between micro- and meso-pores is that adsorption in the former is mainly a process of pore-filling [19] and the adsorbed phase volume coincides with the pore volume. On the other hand, a mesopore can accommodate both the adsorbed and bulk phase simultaneously and its diameter is at the length-scale at which condensation transitions under confinement can occur. This gives rise to known features, such as the appearance of sub-critical hysteresis loops [18], and affects the criticality of fluids in the pores [20].

Modern methods of Density Functional Theory (DFT) and Monte Carlo simulations (MC) are available to obtain accurate pore-size distributions (PSD) of carbonaceous adsorbents over the entire micro- and mesopore range [8,21]. To minimise computing demand, the deployment of these numerical approaches is generally limited to pores of simplified geometry (e.g., slits) [11]; an adsorption isotherm is then constructed using the weighted linear combination of isotherms computed for pore-classes of varying widths. Such analysis is largely based on the subcritical physisorption of N_2 and/or Ar at their standard boiling point (77 K and 87 K, respectively), because at these conditions the condensation pressure is an explicit function of the pore size. However, there are compelling arguments in favour of extending textural analysis with additional gases and/or thermodynamic conditions, including (i) kinetic restrictions that are inherently present in micropores at cryogenic temperatures [22]; (ii) the need to mimic the conditions of the specific industrial application [23]; and (iii) the validation of the obtained pore-structural information over a range of conditions, from sub- to super-critical adsorption [9,11,24]. As a matter of fact, a more robust approach to PSD analysis could be obtained by a combination of sub- and super-critical adsorption data [25], as the latter also show pore-size dependent adsorption behaviour [19,26,27]. However, attempts of using measurements at supercritical conditions for the characterisation of porous carbons have been limited to systems that are predominantly microporous [10,23,24,28,29] and have been so-far only partly successful. We attribute this last observation to (i) the almost exclusive use of slit-pores in theoretical adsorption models and (ii) the lack of supercritical adsorption measurements over the range of conditions required to characterise the distribution of both micro- *and* meso-pores.

Supercritical adsorption has been studied experimentally, but the data set on industrially important materials that contain significant levels of mesoporosity remain scattered. Experimental adsorption isotherms on carbon surfaces are largely limited to (micro)porous activated carbons [27,30–36], the only exception being the seminal work by Specovious and Findenegg on graphitised carbon black [19]. Most of the work on ordered mesoporous solids has focused on silicas, including Controlled Pore Glass (CPG) [20,37], SBA-15 [38,39], MCM-41 [36] and aerogels [40]. These studies have revealed that supercritical adsorption produces characteristic confinement effects related to the formation of a thick adsorbed layer in mesopores — up to two to five molecular diameters of the adsorbate [19,27]. The effect can be sustained up to about 10 K above the critical temperature of the adsorbate (T_c) [19] and its strength depends largely on the pore-wall curvature [20,37]. A practical implication is that the measured excess adsorption isotherms do not exhibit the same features observed on microporous adsorbents, namely an early maximum followed by a linear fall with increasing bulk density [41]. Rather, the maximum of the excess amount adsorbed is shifted towards higher densities (above 5 mol/L), its value increases markedly with decreasing temperature and the descending part of the isotherm is far from being linear [19]. These attributes suggest that textural properties of the

adsorbents can in principle be inferred from a supercritical adsorption isotherm. Most importantly, they also indicate that in this endeavour, theoretical approaches are needed where adsorbate–adsorbent *and* adsorbate–adsorbate interactions are explicitly accounted for [20,26], as opposed to the use of simplified macroscopic adsorption models that are commonly applied to describe supercritical adsorption isotherms [42].

In this study, we report a comprehensive set of supercritical unary adsorption isotherms of CO_2 and CH_4 measured on a commercial mesoporous carbon up to 25 MPa at 40 °C, 60 °C and 80 °C. Results are presented in terms of excess adsorption isotherms and key adsorption metrics are extracted from the measurements, including Henry constants and CO_2/CH_4 selectivities as a function of temperature. The complete set of isotherms is described using a model based on the lattice DFT formalism that has been newly developed here for pores of cylindrical geometry. To this aim, the adsorbent's PSD obtained by Ar (87 K) physisorption analysis was used to identify representative pore classes from the calibration of the lattice DFT model against supercritical data measured at the lower temperature ($T/T_c = 1.03$). The general applicability of our experimental and modelling workflow is validated by extending the analysis to a literature data set on a microporous activated carbon.

2. Experimental

We consider two adsorbent materials, namely a mesoporous carbon (MC) and a microporous activated carbon (AC). For the latter, a comprehensive data set of supercritical adsorption isotherms of CH_4 and CO_2 is reported in the literature [33,43], which we have used in this study to evaluate the general applicability of our experimental and modelling workflow. The former includes the measurement of (i) subcritical adsorption measurements for the textural characterisation of the adsorbent and (ii) supercritical adsorption isotherms for ascertaining adsorption capacities over a wider range of pressure and temperatures. A lattice DFT model is applied at each stage of the analysis, thereby enabling (i) the extraction of representative pore-sizes of the adsorbent, (ii) the description of the supercritical adsorption isotherms and (iii) the estimation of useful thermodynamic parameters, such as the Henry constants and the isosteric heat of adsorption. The details of this workflow are described in the following sections.

2.1. Materials

Graphitised mesoporous carbon (MC, powder, $45 \pm 5\,\mu m$ particle size, $10 \pm 1\,nm$ average pore diameter) and Activated Charcoal Norit (AC, RB3, 3 mm rods) were purchased from Sigma-Aldrich and used as provided. Textural characterisation by physisorption analysis was carried out on both carbon samples (Section 2.2), while supercritical adsorption experiments were only conducted on MC (Section 2.3), because of the availability of a comprehensive literature data set on the AC Norit [33,43]. The skeleton density of the adsorbents are $1.688\ g/cm^3$ (MC) and $1.943\ g/cm^3$ (AC). The former has been estimated from a helium buoyancy experiment carried out at 80 °C (see Section 2.3), while the latter is the value reported in [43], which has been obtained upon describing helium adsorption isotherms using a suitable equation of state. This last approach is deemed to be more suitable for microporous solids, because helium adsorption can lead to an underestimation of the true skeleton volume, if the experiment is not carried out at a temperature that is sufficiently high [44]. Amorphous carbon is reported to have a density in the range 1.8–2.1 g/mL [45] and the difference observed here is thus not surprising. This range can be wider for mesoporous carbons, because of the utilisation of different precursors for their synthesis. Values similar to the one observed here (1.7 g/mL) have been explained by the presence of non-accessible voids as well as hetero-atoms within the carbon framework [46].

The gases used in this study were procured from BOC, namely CO_2, Ar and He at purities of 99.999% and N_2 at a purity of 99.9992%; for the supercritical adsorption experiments, CO_2 and CH_4 were purchased at a purity of 99.995% and 99.5%, respectively. The critical properties of the pure adsorbates are as follows: $T_c(CO_2)$ = 304.1 K, $P_c(CO_2)$ = 7.37 MPa, $\rho_c(CO_2)$ = 10.62 mol/L [47]; $T_c(CH_4)$ = 190.6 K, $P_c(CH_4)$ = 4.60 MPa, $\rho_c(CH_4)$ = 10.14 mol/L [48].

2.2. Subcritical adsorption

A Quantachrome Autosorb iQ was used to measure subcritical adsorption isotherms on the two materials in the pressure range 1×10^{-7} – 0.1 MPa using Ar at 87 K (on MC and AC) and N_2 at 77 K (on MC). The two adsorptives are equally suitable for the characterisation of MC, while Ar is expected to provide a more reliable assessment of microporosity in AC [22]. Additional measurements were carried out on MC using CO_2 at 273 K, 283 K and 298 K to extend the temperature range covered in the high pressure measurements for estimating the Henry constants. Prior to the experiments, each sample was loaded in the equipment's external degassing station, where vacuum was applied throughout the following temperature ramp: 25 °C (10 min), 60 °C (1 h), 90 °C (1 h), 120 °C (16 h). The sample was then transferred to the measuring station, where a measurement with helium was conducted to estimate the void volume of the measuring cell, followed by the measurement with the selected adsorptive in both adsorption and desorption mode. In the experiments with MC, 0.15 g (N_2 and Ar) and 1.05 g (CO_2) of adsorbent were used, while 0.06 g were used for the experiments with Ar on AC. The experimental data were interpreted upon application of the non local DFT model (NLDFT), available within the instrument software, to obtain the pore size distribution, specific surface area and total pore volume of the adsorbents. To this aim, the carbon model for cylindrical pores was selected to fit the desorption branch of the measured N_2 and Ar isotherms.

2.3. Supercritical adsorption

CO_2 and CH_4 adsorption isotherms were measured gravimetrically at 40 °C, 60 °C and 80 °C using a Rubotherm Magnetic Suspension Balance (MSB) in the pressure range 0–250 bar. The MSB provides high-resolution (10 μg) weight measurements from which both the excess amount adsorbed and the bulk density of the adsorbate are extracted [49]. Fig. 1 shows a schematic of the experimental setup that includes the MSB in addition to various ancillary components, namely (i) the control unit that also houses two pressure transmitters (Model 33X by Keller UK Ltd.) for moderate (<35 bar) and high-pressure measurements (<700 bar) both at 0.01% full-scale accuracy; (ii) one liquid thermostat (Model 25F by Julabo GmbH) that controls the temperature in the measuring chamber (±0.01 °C); (iii) one syringe-pump (Model 500D by Teledyne ISCO) to achieve and maintain a constant pressure in the measuring chamber beyond cylinder pressure; (iv) a rotary vane vacuum pump (Model RZ 2.5, Vacuubrand) for taking measurements below atmospheric pressures and for regenerating the adsorbent. The components of the experimental system are connected with stainless steel tubing and hand valves (SITEC, Sieber Engineering AG).

After loading 1.224 g of sample (MC) in the measuring chamber, a degassing procedure was carried out by heating the system to 120 °C and pulling vacuum for at least 7 h. This was followed by recording a vacuum point at 80 °C in the two measuring positions ($MP_{1,0}$ = $m_s + m_{met}$ and $MP_{2,0} = MP_{1,0} + m_{sk}$), where m_s, m_{met} and m_{sk} are the mass of the adsorbent, the lifted metal parts and the calibrated sinker, respectively. Helium was then charged into the system to obtain weight measurements ($MP_{1,He}$ and $MP_{2,He}$) at 80 °C and eleven pressure points in the range 1.5 bar to 136 bar (with an equilibration of about 1 h for each point). These data were used to estimate the combined skeletal

volume of the adsorbent and the lifted metal parts, $V_0 = V_s + V_{met}$, using the following equation:

$$MP_{1,He}(\rho_b, T) = MP_{1,0} - \rho_b V_0 \tag{1}$$

where ρ_b is the density of the bulk fluid obtained by combining weight measurements in the two measuring positions (using a calibrated titanium sinker, see below). After evacuating the measuring chamber and purging the rest of the system with the selected adsorbate (CO_2 or CH_4), adsorption isotherms were measured by filling the chamber at various pressures and allowing the system to equilibrate for at least 60 min. Overnight measurements were regularly acquired to confirm the absence of significant adsorption (or desorption) beyond the chosen equilibration time. Also, no hysteresis was observed between adsorption and desorption points for the temperatures and pressures investigated in this study, and most isotherms points were thus taken in desorption mode. After the completion of the measurements with CO_2, the sample was again regenerated in-situ while heating to 120 °C and pulling vacuum for at least 7 h. Another vacuum point was taken, followed by adsorption measurements with CH_4 (following the same protocol as above).

At each pressure point, the MSB software automatically cycles between the zero point and the two measuring points MP_1 and MP_2, with a settling time of 30 s, 1.5 min and 30 s, respectively. All measurements are logged and, for each pressure and temperature combination, the average of the last five readings was taken as the equilibrium point. The following two equations are used to compute the bulk density of the adsorbate and the excess amount adsorbed:

$$\rho_b = \frac{(MP_{2,0} - MP_{1,0}) - (MP_2(\rho_b, T) - MP_1(\rho_b, T))}{V_{sk}} \tag{2a}$$

$$n^{ex} = \frac{MP_1(\rho_b, T) - MP_{1,0} + \rho_b V_0}{M_w m_s} \tag{2b}$$

where M_w is the molecular weight of the adsorptive and V_{sk} is the volume of the calibrated titanium sinker. As described in the Supplementary Information (SI), Eq. (2) is used to estimate the uncertainty associated with the measured bulk density and excess amount adsorbed following classic formula of error propagation that include contributions from the observed standard deviation of the measured weights, the sinker volume (4.364 ± 0.002 cm^3 at 67% confidence) and the estimated value of V_0 (1.392 ± 0.001 cm^3 at 67% confidence). The latter represents the main driver of the uncertainty associated with supercritical adsorption measurements at elevated pressures. For the data reported in this study, the uncertainty on n^{ex} was found to range between 0.47–21 μmol/g and 2.1–12 μmol/g at 67% confidence for CO_2 and CH_4, respectively. These estimates are in line with those reported in the literature for measurements carried out on porous materials using Magnetic Suspension Balances [41,50].

3. Modelling

3.1. Lattice DFT model for cylindrical pores

The model used in this study belongs to the class of lattice-gas models, also referred to as the lattice Density Functional Theory (lattice DFT) [51,52]. The theory approximates the adsorbent using a distribution of properly weighted model pores of simple geometries (e.g., slit, channels or cages), whose internal space is discretised, so that fluid molecules form a regular pattern (a lattice). This coarse-graining facilitates considerably the estimation of the density profile within the pore, as opposed to standard implementations of DFT, which are computationally expensive to implement [18]. In addition to incorporating information about the adsorbent geometry, the lattice DFT model considers both adsorbate–adsorbate and adsorbate–adsorbent interactions, thereby enabling the description of a wide spectrum of adsorption isotherms and behaviours [53]. With relevance to this study,
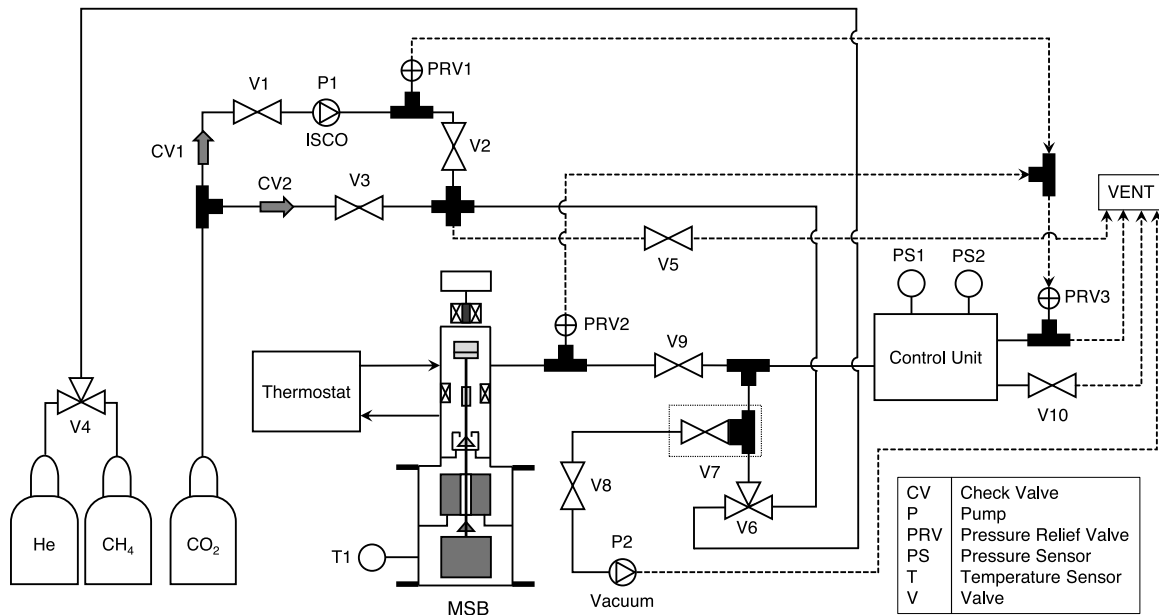
Fig. 1. The experimental setup used in this study for supercritical adsorption measurements with CO_2 and CH_4 in a Rubotherm Magnetic Suspension Balance (MSB).

the lattice DFT approach has been shown to correctly capture the adsorption of supercritical fluids on both micro- and meso-porous adsorbents, without requiring any assumption of the density of the adsorbed fluid [26,54–56]. While in these previous studies the analysis was mostly restricted to either 1D slit or 2D pore channels, we consider here cylindrical pores to provide a more realistic representation of the carbonaceous adsorbents used in this study. We note that cylindrical pores were previously used by Qajar and co-workers [57] to describe N_2 adsorption on shale and coal, but their study was limited to subcritical conditions; we build on these developments by deriving in the following the relevant operating equations for supercritical gas adsorption.

We consider a cylindrical pore with a cubic lattice to accommodate fluid molecules, as shown in Fig. 2. To facilitate the description of the mathematical formulation of the model, we compare the cylindrical pore to a rectangular channel (image on the left-hand side) with the same number of lattice sites (four lattice layers are shown in the example and represented by the dashed lines). In our treatment, $j = 1$ and $j = J$ represent the central and outer (wall) layer, respectively, and the radius of each layer, r_j, is defined as follows:

$$r_j = \begin{cases} d/2 & \text{for } j = 1 \\ (j-1)d & \text{for } j > 1 \end{cases} \tag{3}$$

where d is the diameter of the lattice site, which in our study is taken as the collision diameter of the gas molecule ($\sigma_{CO_2} \approx \sigma_{CH_4} \approx 4$ Å). The pore diameter is therefore readily obtained as, $D_{p,J_k} = d(2J - 1)$, and its volume is defined as follows:

$$v_{p,J} = \pi d^2 L \left[\frac{1}{4} + 2 \sum_{j=2}^{J} (j-1) \right] \tag{4}$$

where L is the length of the pore (see the SI for additional details on the derivation of this equation). With reference to the generic three-dimensional formalism presented by Hocker et al. [26], the Ono–Kondo lattice equations for a molecule in a cylindrical pore with J lattice layers are:

$$0 = \varepsilon_{ff}(z_j^{a+}\theta_{j+1} + z_j^s\theta_j - z^b\theta_b) + k_B T \ln\left[\frac{\theta_j(1-\theta_b)}{\theta_b(1-\theta_j)}\right] \quad \text{for} \quad j = 1$$

$$0 = \varepsilon_{ff}(z_j^{a+}\theta_{j+1} + z_j^{a-}\theta_{j-1} + z_j^s\theta_j - z^b\theta_b) + k_B T \ln\left[\frac{\theta_j(1-\theta_b)}{\theta_b(1-\theta_j)}\right]$$
$$\text{for} \quad 1 < j < J \tag{5}$$

$$0 = \varepsilon_{sf}z_j^{a+} + \varepsilon_{ff}(z_j^{a-}\theta_{j-1} + z_j^s\theta_j - z^b\theta_b) + k_B T \ln\left[\frac{\theta_j(1-\theta_b)}{\theta_b(1-\theta_j)}\right]$$
$$\text{for} \quad j = J$$

where θ_b is the probability of occupancy in the bulk and θ_j is the probability of having layer j occupied. This probability is interpreted as the degree of occupancy and can be translated into a corresponding density (bulk or adsorbed-phase) using a suitable mapping function (see below). The equations also include k_B (the Boltzmann's constant), T (the temperature), ε_{ff} (the adsorbate–adsorbate interaction energy) and ε_{sf} (the adsorbate–adsorbent interaction energy). In this formulation, these interactions are confined to the nearest neighbouring molecules by using a set of coordination numbers, namely z^b (bulk), z_j^s (same layer), z_j^{a+} (outer adjacent layer) and z_j^{a-} (inner adjacent layer), for which the following general relationship holds:

$$z^b = z_j^s + z_j^{a+} + z_j^{a-} \quad \text{for all } j \tag{6}$$

For a cubic lattice in a slit pore, $z^{a+} = z^{a-} = z^a$ and the coordination numbers do not depend on the position, j, i.e. $z^b = 6$, $z^s = 4$ and $z^a = (z^b - z^s)/2 = 1$. In a cylindrical pore, however, the capacity of each layer increases when moving from the centre of the pore to the pore wall; accordingly, the two coordination numbers with the adjacent layers can be expressed as the ratio of the perimeters of the relevant layers:

$$z_j^{a+} = \frac{r_{j+1}}{r_j} = \frac{j}{j-1} \quad \text{for } j > 1$$

$$z_j^{a-} = \frac{r_{j-1}}{r_j} = \frac{j-2}{j-1} \quad \text{for } j > 2 \tag{7}$$

which thus correspond to the ratio of the number of sites between two adjacent layers (note also that $z_j^{a-} = 1/z_{j-1}^{a+}$); once these have been computed, the corresponding value for z_j^s is found from Eq. (6) ($z^b = 6$). The only exception to Eq. (7) is for layers 1 and 2, as the former is the only layer where the radius is defined at the edge, rather than the
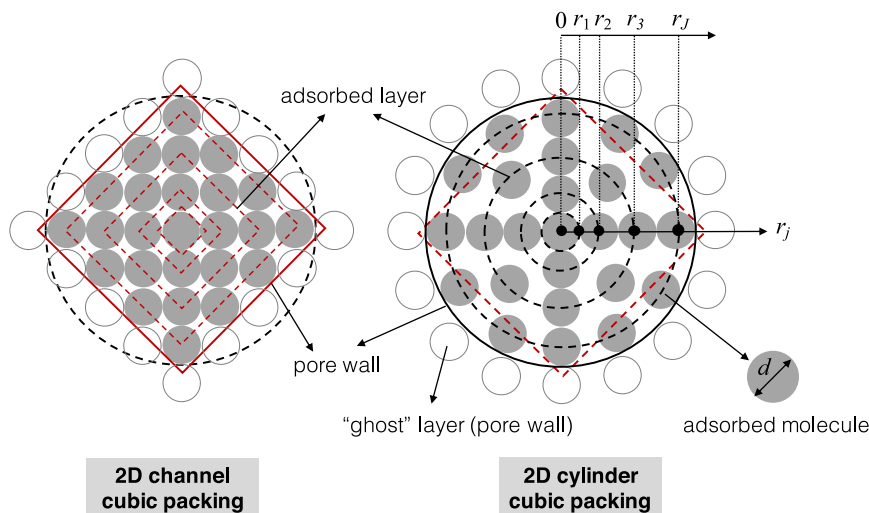
Fig. 2. Depiction of a cylindrical pore considered in the lattice DFT framework. Circles represent adsorbed molecules with diameter d and lattice layers are denoted by the distance, r_j, from the centre of the pore of diameter $d(2J - 1)$, where J is the total number of layers.

centre of the lattice site. In particular, for $j = 1$, $z_1^{a+} = 4$ and $z_1^{a-} = 0$; accordingly, $z_1^s = 2$ to satisfy Eq. (6). For $j = 2$, $z_2^{a+} = 2$ (Eq. (7)) and $z_2^{a-} = 1/z_1^{a+} = 1/4$; consequently, $z_2^s = 3.75$ to satisfy Eq. (6). For layers $j > 2$, the lateral coordination number, z^s, is always 4. It is worth highlighting that the unique features of the cylindrical geometry are also accounted for in the *effective* surface energy term in Eq. (5), $\varepsilon_{sf} z_J^{a+}$, where z_J^{a+} refers to the coordination with a "ghost" layer at the wall of the pore. The term accounts for the enhanced adsorbate–adsorbent interaction due to the curvature of the wall relative to a flat surface and introduces a dependency of the strength of such interaction on the size of the pore. Accordingly, when more than one pore-class is considered, the *average* adsorbate–adsorbent interaction is obtained as their weighted average:

$$\bar{\varepsilon}_{sf} = \sum_{k=1}^{K} w_k \varepsilon_{sf} z_{J_k}^{a+} \tag{8}$$

where J_k is the number of layers in the pore-class k and w_k is its surface area fraction, obtained directly from the textural characterisation by physisorption.

3.1.1. From lattice to physical units

A mapping function is used to convert the occupancy values obtained from the lattice model to density:

$$\rho = \frac{\rho_{\max} \rho_c \theta}{\rho_{\max}(1 - \theta) - \rho_c(1 - 2\theta)} \tag{9}$$

This function satisfies three important physical constraints [26]: (i) for $\theta = 0$, $\rho = 0$; (ii) for $\theta = 1$, $\rho = \rho_{\max}$ (maximum packing density when the lattice is fully occupied); (iii) for $\theta = 0.5$, $\rho = \rho_c$ (critical density of the fluid at half occupancy). Once the density values in each layer are known, the total excess amount adsorbed per unit mass of adsorbent can be computed as follows:

$$n^{ex} = c_{sat} \sum_{k=1}^{K} \frac{v_{p,k}}{\left[\frac{1}{4} + J_k(J_k - 1)\right]} \left[\frac{1}{4}(\rho_1 - \rho_b) + 2\sum_{j=2}^{J_k}(\rho_j - \rho_b)(j - 1)\right] \tag{10}$$

where ρ_j is the density in layer j of pore class k (complete derivation in the SI). In Eq. (10), the total specific pore volume of the adsorbent is discretised into K pore classes, each with a different specific pore volume, $v_{p,k}$, and pore size (or number of layers, J_k), i.e. $v_p^{tot} = \sum_{k=1}^{K} v_{p,k}$. Note that a temperature-dependent saturation capacity factor, $c_{sat} \in [0, 1]$, has been introduced to account for a reduction of the volume occupied by the supercritical adsorbed phase at $\rho = \rho_{\max}$ as compared to a close packing of molecules. The total pore volume occupied by the

adsorbed phase at "saturation" is thus obtained as $c_{sat} v_p^{tot}$. We note that because the saturation factor is defined based on the pore volume of the adsorbent, it applies to both absolute and excess adsorption.

3.1.2. Solution procedure

The solution to the lattice DFT model is obtained by solving the set of non-linear equations, Eq. (5), for the occupancy θ_j at specified θ_b. The function lsqnonlin in MATLAB was used to solve the equations with default parameters of the termination tolerance (1×10^{-6}) and maximum number of iterations (400). The occupancy values are converted to density values using Eq. (9), which are in turn used in Eq. (10) to compute the excess amount adsorbed. The following model parameters are specified: (i) a cubic lattice pattern ($z^b = 6$, z^s, z^{a-} and z^{a+} defined above); (ii) the adsorbate–adsorbate interaction energy, $\varepsilon_{ff} = -4k_B T_c/z^b$; (iii) the temperature (T); (iv) the measured total specific pore volume of the adsorbent, v_p^{tot}, and its discretisation in K representative pore classes (as detailed below). For each adsorbate, the remaining parameters were found by fitting the model to the experimental data, namely (i) the adsorbent–adsorbate interaction energy, ε_{sf}, (ii) the maximum density in the lattice, $\rho_{\max}$ and (iii) the temperature-dependent saturation factor, c_{sat}. The function fminsearch in MATLAB was used to minimise the following objective function (specified function and parameter tolerance level of 1×10^{-6}):

$$\Phi = \sum_{t=1}^{T} \sum_{p=1}^{P} \left[n_{exp}^{ex}(t, p) - n_{mod}^{ex}(t, p)\right]^2 \tag{11}$$

where n_{exp}^{ex} is the measured experimental point at a specific temperature, t, and density, p, and n_{mod}^{ex} is the corresponding amount obtained from the model.

The discretised PSD used in the lattice DFT model was obtained from Ar physisorption at 87 K. To identify the representative pore classes, only the excess adsorption isotherm measured with CO_2 at 40 °C was considered. To this aim, a fixed number of pore classes were used as additional fitting parameters, while constraining their volume, $v_{p,k}$, to the experimentally-obtained PSD. In particular, the pore volume allocated to a given pore class k with J_k layers was obtained as the sum of the pore volume in the range $[v_{p,k}, v_{p,k+1}]$, with the exception of the smallest pore class, for which $v_{p,k}$ represents the cumulative specific pore volume up to that pore size. The number of classes, K, was selected by applying the fitting procedure iteratively for increasing number of pore classes until the improvement in the value of the objective function was too minor to warrant an additional parameter.

The objective function was minimised using the genetic algorithm (ga) available in the MATLAB global optimisation toolbox. The population size was 100 times the number of fitted parameters and the number of generations were 100 (although often less generations were required to achieve the default tolerance level of 1×10^{-6}). Lower and upper bounds were specified for the fitting and these were progressively narrowed on the basis of the optimal parameters, to achieve a lower value for the objective function Φ. Only integer values were considered for the number of layers, J_k, and a penalty was specified if two classes had the same number of layers. This reduced distribution of pores was then used to describe the adsorption of CO_2 at the other temperatures and the full set of CH_4 isotherms.

3.2. Henry constants and isosteric heat of adsorption

Henry constants were obtained by fitting the experimental excess adsorption isotherms with the Virial equation:

$$\ln(f/n^{ex}) = \sum_{i=0}^{m} C_i(n^{ex})^i \tag{12}$$

where f is the fugacity and C_i are the Virial coefficients; the temperature-dependent Henry constant is thus obtained as $H = \exp(-C_0)$. For Eq. (12) to be valid, only the points measured up to moderate pressures were considered, (i.e. up to ~ 4.8 MPa for CO_2 and ~ 7.0 MPa for CH_4 depending on the temperature); at these conditions, the value of the gas bulk density is less than 10% of the density of the saturated liquid 21.073 mol/L for CO_2 and 26.327 mol/L for CH_4 [58], and excess and absolute amount adsorbed are effectively equal. For both adsorbents, the first two Virial coefficients were found to be sufficient to describe the data; this was additionally validated by a plot of $\ln(f/n^{ex})$ vs. n^{ex}, which yields a linear region from which the Henry constant can be extrapolated. The integrated van't Hoff equation is then used to describe the temperature dependence of the Henry constant [14]:

$$H = H_0 \exp\left[-\Delta h_0/RT\right] \tag{13}$$

which enables the graphical estimation of the (experimental) isosteric heat of adsorption at zero coverage, Δh_0, from the so-called van't Hoff plot ($\ln(H)$ vs. $1/T$).

Estimates of these properties can also been obtained from the lattice DFT model. In particular, it can be readily shown (see SI) that Eq. (5) reduces to Henry's law at sufficiently low concentrations ($\theta_b \to 0$ and $\theta_J \ll 1$):

$$\theta_J = H'_J\theta_b \tag{14}$$

where $H'_J = \exp\left[-\epsilon_{sf} z_J^{a+}/k_BT\right]$ is the dimensionless Henry constant. Upon application of the mapping function, Eq. (9), and combination with Eq. (10), the following expression for the Henry constant (in units of mmol g^{-1} bar^{-1}) is obtained that includes contributions from each pore-class k:

$$\widetilde{H} = \widetilde{H_0}\frac{100}{RT}c_{sat}\sum_{k=1}^{K}\frac{2\nu_{p,k}(J_k-1)}{\left[\frac{1}{4}+J_k(J_k-1)\right]}\exp\left(\frac{-\epsilon_{sf}z_{J_k}^{a+}}{k_BT}\right) \tag{15}$$

where $\widetilde{H_0}$ is a dimensionless pre-exponential constant, $R = 8.314$ J/mol K is the gas constant, the temperature T is in the units of Kelvin and the specific pore volume, $\nu_{p,k}$ is given in units of cm^3/g. Accordingly, the isosteric heat of adsorption at zero coverage, $\Delta\widetilde{h_0}$, can be obtained upon application of the van't Hoff equation on the computed values of $\widetilde{H}$. We note that $\Delta\widetilde{h_0}$ includes contributions from both the absorbate–adsorbent interaction parameter, ϵ_{sf}, and the temperature-dependent pore-saturation factor, c_{sat}. Accordingly, linearity on the van't Hoff plot requires that $\ln(c_{sat}) \sim 1/T$.

Table 1

Textural properties of MC and AC obtained upon fitting the carbon NLDFT model for cylindrical pores to subcritical N_2 (77 K) and Ar (87 K) adsorption data. Properties reported for the AC Norit R1 used in this study for the analysis of supercritical adsorption isotherms are also given, including SSA [33] and ν_{tot} [43].

Material	Adsorbate	SSA (m^2/g)	ν_{mic} (cm^3/g)	ν_{mes} (cm^3/g)	ν_{tot} (cm^3/g)
MC	Ar	218	0.003	0.452	0.456
	N_2	219	0.008	0.437	0.445
AC (Norit RB3)	Ar	1790	0.461	0.171	0.632
AC (Norit R1)	N_2	1339	–	–	0.605

4. Results

4.1. Textural characterisation by subcritical adsorption

The results of the physisorption analysis on the two carbonaceous adsorbents are presented in Fig. 3, including N_2 (77 K) and Ar (87 K) adsorption/desorption isotherms, and the PSD calculated from their desorption branches. The characteristic features of the two porous carbons are readily visible in Fig. 3a: adsorption on MC starts with a modest amount of micropore filling at very low pressures ($P/P_0 < 0.01$), indicating the presence of some microporosity. It then proceeds with the formation of a monolayer in the mesopores, which is completed at the first inflexion point ($P/P_0 \approx 0.3$); multilayer adsorption ensues and continues until the onset of the second plateau indicating that mesopore filling has concluded ($P/P_0 \approx 0.9$). The measurements with N_2 and Ar show a qualitatively similar behaviour, but the isotherms of the latter are shifted to larger values due to its larger liquid density at saturation ($\rho_{liq} = 34.91$ mol/L vs. $\rho_{liq} = 28.84$ mol/L). Based on the IUPAC classification [22], MC shows Type IV(a) behaviour with hysteresis of Type H1 ($0.56 < P/P_0 < 0.96$), which is characteristic of porous adsorbents with a narrow range of uniform mesopores. The Ar isotherm measured on AC is of Type I(b) and shows a steep uptake at very low pressures, followed by a gradual approach towards a limiting adsorption value that indicates early completion of (micro)pore filling ($P/P_0 \approx 0.2$). This is confirmed by the presence of a modest Type H4 hysteresis loop at $P/P_0 > 0.4$, which is often observed in micro-mesoporous carbons [22]. The larger total Ar adsorption of AC (506 cm^3(STP)/g) as compared to MC (376 cm^3(STP)/g) indicates a larger total pore volume.

The experimental adsorption isotherms have been fitted using the carbon NLDFT model for cylindrical pores to obtain quantitative estimates of pore volumes and their distribution. As shown in Fig. 3a, the model (solid lines) describes accurately the experimental data (desorption branch) on both adsorbents, with a fitting error below 1% for each gas and adsorbent. The obtained values for the specific surface area (SSA), micro- (ν_{mic}, $D_p < 2$ nm), meso- (ν_{mes}, $D_p = 2 - 50$ nm) and total pore volume ($\nu_{tot} = \nu_{mic} + \nu_{mes}$) are reported in Table 1. It can be seen that the results obtained on MC using Ar and N_2 are in excellent agreement, with deviations on the obtained SSA and ν_{tot} of 0.8% and 2.4%, respectively. Mesopores contribute to more than 98% of the total pore volume and the data also agree with specifications provided by the supplier, i.e. $\nu_{tot} \approx 0.5$ cm^3/g and SSA $\approx 150 - 250$ m^2/g [59]. The total pore volume of AC is about 40% larger than the value computed for MC and is mostly contained in the micropores ($\sim 70\%$vol.). Notably, both the total pore volume and specific surface are higher than literature values reported for N_2 physisorption analysis ($\nu_{tot} = 0.40 - 0.50$ cm^3/g and SSA = $697 - 1220$ m^2/g) [60–63]. This observation supports the common perception that Ar is more suited to the assessment of microporosity as compared to N_2, which is affected by limited diffusion at the conditions of the experiments [22]. Our results on AC Norit RB3 agree reasonably well with properties reported for the AC Norit R1 used in this study for the analysis of supercritical adsorption, namely $\nu_{tot} = 0.605$ cm^3/g [43] and SSA = 1339 m^2/g [33].
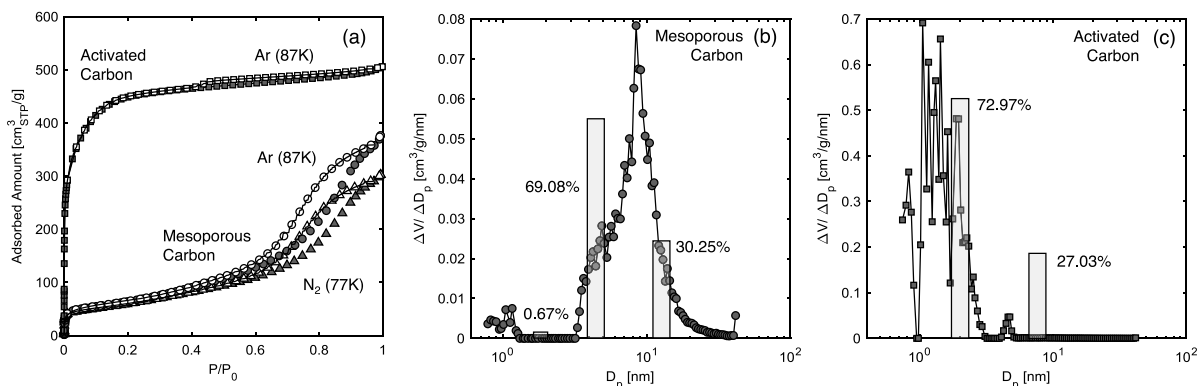
Fig. 3. Physisorption analysis on mesoporous carbon (MC) and activated carbon (AC). (a) N_2 (77 K) and Ar (87 K) adsorption isotherms measured in both adsorption (filled symbols) and desorption (empty symbols) mode. The PSD calculated from the desorption branch of the Ar data for (b) MC and (c) AC using the NLDFT carbon model for cylindrical pores. The bars represents the discretised PSD obtained from the lattice DFT model; for MC, the selected pore sizes, D_p, corresponds to cylindrical pores with $J = 2$ (0.67 vol%), 6 (69.08 vol%) and 15 layers (30.25 vol%). For AC, the selected pore sizes corresponds to cylindrical pores with $J = 3$ (72.97 vol%) and 11 (27.03 vol%). STP conditions are defined as 273.15 K and 1 atm. P_0 is the saturation pressure at the measurement temperature ($\sim$ 760 torr).

4.2. Textural characterisation by supercritical adsorption

The material's PSD obtained from the analysis described in the previous section is presented in Fig. 3b (MC) and c (AC); it can be seen that the former possesses a rather narrow distribution of mesopores centred at about 8.4 nm, while the latter is dominated by micropores (<2 nm) and small mesopores (3–5 nm). The bars plotted alongside the computed PSD are the representative pore-classes obtained upon fitting the cylindrical lattice DFT model to the supercritical adsorption isotherm measured at 40 °C with CO_2 on both materials. The corresponding model fits are shown in Fig. 4 together with the individual contribution from each pore class to the total excess amount adsorbed. Starting from an initial population of 4 pore-classes, the lattice DFT model identified that three (MC) and two (AC) pore-classes are sufficient to accurately describe the supercritical adsorption isotherm over the full range of density values ($0 < \rho/\rho_c < 2.25$, corresponding to pressures up to 25 MPa for MC and 50 MPa for AC). For MC these classes are associated to pores of size 1.2 nm, 4.4 nm and 11.6 nm, and for AC to pores of size 2 nm and 8.4 nm. The key observation from Fig. 4 is that, similarly to the physisorption analysis applied to subcritical isotherms, also isotherms measured slightly above the critical point of the fluid ($T/T_c = 1.03$ in this case) manifest pore-size dependent adsorption behaviour, which is reflected in the shape of the isotherms. In particular, the isotherm measured on MC is dominated by the characteristic late filling of mesopores ($J = 5$ and 12) that results in the maximum excess amount adsorbed being attained at a relatively large bulk density ($\rho_b \approx 6$ mol/L). On the contrary, the isotherm measured on AC is dominated by the early filling of micropores ($J = 3$) and only partly by the filling of the mesopores ($J = 10$), and the maximum excess amount adsorbed is observed at a much lower bulk density ($\rho_b \approx 3$ mol/L). Moreover, beyond its maximum point, the isotherm measured on MC is concave, while the one measured on AC is more linear and reminiscent of the behaviour observed with microporous adsorbents [41]. This behaviour can be traced back to the definition of the excess amount adsorbed ($n^{ex} = n^a - \rho_b V^a$), which implies a linear dependency with bulk density upon attainment of adsorption saturation (complete micropore filling, with n^a and V^a approaching a constant value). This sensitivity at (slightly) supercritical conditions of the adsorption behaviour to the characteristic pore-structure of the material offers a complementary tool for the textural characterisation of porous materials, enabling the identification of those pore classes that have the strongest contribution to supercritical adsorption.

4.3. CO_2 and CH_4 supercritical adsorption on mesoporous carbon

Unary excess adsorption isotherms measured with CO_2 and CH_4 on MC at temperatures of 40 °C, 60 °C and 80 °C are shown in Fig. 5a

as a function of bulk density. In Fig. 5b are plotted the corresponding bulk density values measured in-situ alongside data reported by NIST (shown as solid lines). An excellent agreement is observed between the two data sets with an average residual sum of squares of 0.4141 (mol/L)^2 (CO_2) and 0.0008 (mol/L)^2 (CH_4). The results from helium gravimetry, which are used to estimate V_0, are reported in the Supplementary Information. CO_2 adsorbs up to three times more than CH_4 on MC, as a result of the higher-order electric multipole moment of the former that leads to a stronger affinity to the carbon surface [64]. Additionally, we note that the experiments have been carried out at a temperature that is relatively close to the critical temperature of CO_2; this further suggests that in the adsorbed state, CO_2 will have a higher isothermal compressibility than CH_4 leading to a potentially higher selectivity [65]. For both adsorptives, the excess amount adsorbed increases monotonically with density before reaching a maximum value and gradually decreasing with increasing density. For CO_2, the excess amount adsorbed approaches zero at the highest pressure of the experiment, indicating that at these conditions the average density values of bulk and adsorbed fluid are almost identical and the two phases are indistinguishable. The CH_4 isotherms show less of this effect, as such high bulk densities are never achieved at the maximum pressure in our experiment (25 MPa). As expected, the excess amount adsorbed decreases with increasing temperature, due to the exothermic nature of adsorption. Also, a change in temperature has a larger effect on the adsorption of CO_2 as compared to CH_4, due to the relative proximity of the experimental temperature to the critical temperature of the adsorptive. This condition has a strong effect on the adsorbed-phase density within the pores in relation to the bulk fluid density [20,37]. The manifestation of this behaviour can be readily seen in the smoothening of the characteristic peak in the CO_2 isotherms when moving from 40 °C ($T/T_c = 1.03$) to 80 °C ($T/T_c = 1.16$); farther from T_c the peak is no longer visible, as indicated by the CH_4 isotherms ($T/T_c > 1.65$) that show fairly broad maxima. As it will be discussed in Section 4.4, this behaviour is typical of mesoporous materials, for which the excess isotherm shows Type II behaviour (when plotted as a function of pressure) at near-critical conditions, before falling abruptly towards higher densities due to the marked increase in the bulk fluid density [19].

4.4. Lattice DFT modelling of supercritical adsorption on porous carbons

Also shown in Fig. 5 are the results obtained upon fitting the lattice DFT model to the excess adsorption data on MC. The model provides an accurate description of the adsorption isotherms for both gases at all temperatures and over the entire range of bulk densities. The value of the objective function (normalised by the number of
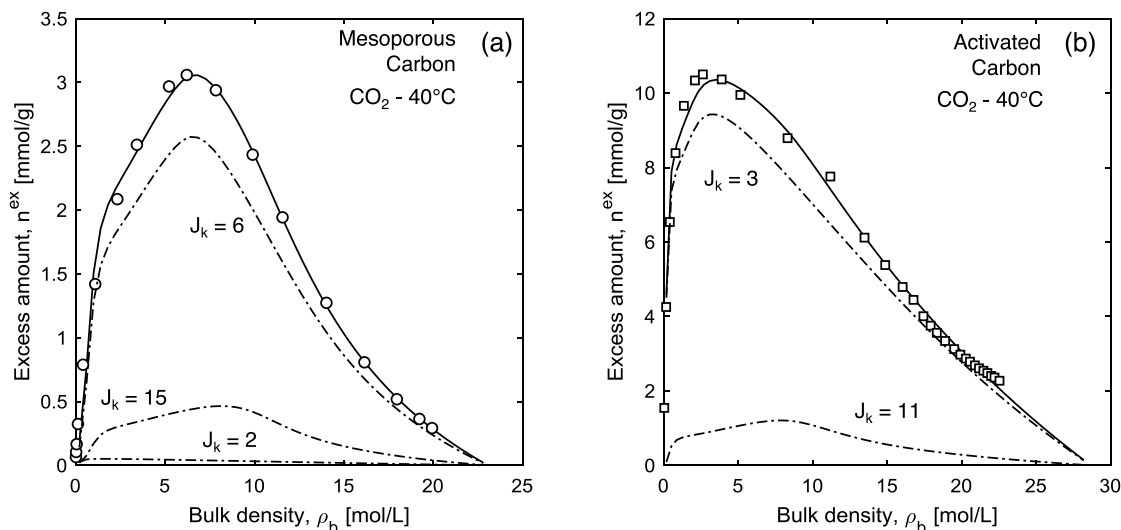
Fig. 4. CO_2 adsorption isotherms at 40 °C for (a) mesoporous carbon (data measured in this study) and (b) activated carbon (data by Ustinov et al. [43]). Symbols represent experimental data, while the solid lines denote optimum fits from the lattice DFT model. The dot-dashed lines are isotherms computed for each pore class k and are labelled in terms of the number of lattice layers J_k.
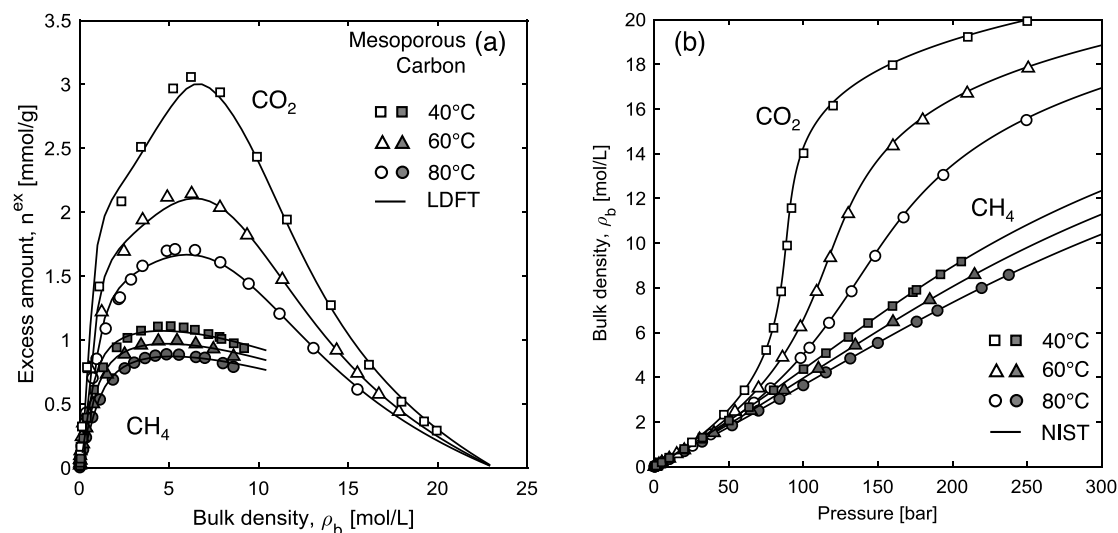

Fig. 5. (a) Unary excess adsorption isotherms measured with CO_2 (empty symbols) and CH_4 (filled symbols) on mesoporous carbon (MC) plotted as a function of the bulk density at 40 °C, 60 °C and 80 °C. $V_0 = 1.392 \pm 0.001$ cm^3 at 67% confidence and $V_{met} = 0.667$ cm^3. Solid lines denote optimum fits from the lattice DFT model (parameter values reported in Table 2). (b) The corresponding bulk density measurements plotted as a function of the measured pressure and their comparison with data reported by NIST (solid lines) [66].

experimental points, N) is $\Phi/N = 0.0096$ (mmol/g)^2 (for CO_2) and 0.0011 (mmol/g)^2 (for CH_4), and is reported in Table 2 together with both input and fitted model parameters. For both gases, the value of the temperature-independent adsorbate–adsorbent interaction parameter, ε_{sf}, is significantly lower than the corresponding average value, $\bar{\varepsilon}_{sf}$, that accounts for both the curvature of the pore-wall and the size of the pore. Interestingly, estimates obtained for CH_4 are systematically higher than those for CO_2, despite the fact that the former shows smaller adsorbed amounts. As anticipated above, supercritical adsorption in mesoporous materials cannot be ascribed solely to the strength of the surface–fluid interaction, because of the possibility of multi-layer adsorption at (slightly) supercritical conditions [19]. This conditions is therefore also strongly controlled by the fluid–fluid interaction parameter, ε_{ff}, whose value for CO_2 is (significantly) larger than for CH_4 (see Table 2).

It is highly instructive to compare the results on MC with those obtained with another carbonaceous porous material with a different PSD. To this aim, we have applied the cylindrical lattice DFT model to literature CO_2 and CH_4 excess adsorption isotherms measured on

AC Norit over a similar range of temperatures (25–70 °C), but wider range of pressures (up to 50 MPa). The obtained model parameter values are also reported in Table 2, while the fitted isotherms are shown in Fig. 6. It can be seen that also in this case the model provides a good description of the experimental data ($\Phi/N = 0.1092$ and 0.0521 (mmol/g)^2 for CO_2 and CH_4, respectively). However, the isotherms differ in many aspects from those obtained on MC: (i) they reach considerably higher excess amounts adsorbed (3 to 5 times); (ii) they are initially much steeper, reaching maximum values at $\rho_b \approx$ 3 mol/L; (iii) beyond the maximum point, they fall almost linearly with bulk density. These features can be attributed to the PSD of the material, which is largely dominated by micropores; as discussed in Section 4.1, micropores become readily filled with adsorbed phase at very low bulk densities and their volume largely determines the (constant) volume of the adsorbed phase [41]. AC also shows a much higher $\bar{\varepsilon}_{sf}$ compared to ε_{sf} (44% increase vs. 24% increase for MC). Again, this is due to its high microporosity, which contributes considerably to the surface area fraction incorporated in the calculation of $\bar{\varepsilon}_{sf}$.

Table 2

Input and fitted parameters of the cylindrical lattice DFT model applied to the description of experimental excess adsorption isotherms measured on mesoporous carbon (MC) and activated carbon (AC). The value of the objective function, Eq. (11) (normalised by the number of experimental points, N) is also given.

Parameter	Mesoporous carbon		Activated carbon	
	CO_2	CH_4	CO_2	CH_4
	Input parameters			
ε_{ff}/k_B [K]	−202.75	−127.04	−202.75	−127.04
σ [nm]	0.40	0.38	0.40	0.38
	Fitted parameters			
ε_{sf}/k_B [K]	−605.16	−714.33	−724.87	−712.36
$\bar{\varepsilon}_{sf}/k_B$ [K]	−749.26	−884.42	−1046.74	−1028.67
ρ_{max} [mol/L]	23.18	31.97	28.86	28.89
	Saturation factor, c_{sat}			
25 °C	–	–	–	0.81
40 °C	0.83	0.34	1.00	0.78
55 °C	–	–	0.96	0.77
60 °C	0.70	0.32	–	–
70 °C	–	–	0.93	0.74
80 °C	0.62	0.30	–	–
Φ/N [mmol/g]^2	0.0096	0.0011	0.1092	0.0521

The lattice DFT also enables the estimation of ρ_{max}, the maximum density in the saturated lattice that would theoretically occur once the bulk fluid density is equal to the adsorbed-phase density (i.e. when n^{ex} is equal to 0). For AC the values predicted for both fluids are very similar, with all excess adsorption isotherms converging towards an estimate of 28.9 mol/L. This results is consistent with the interpretation of the pore-space with a lattice of sites of equal size (reflecting a similar collision diameter of both CO_2 and CH_4 molecules). For MC, the obtained values are 23.2 mol/L (CO_2) and 32.0 mol/L (CH_4). We note that the value for CH_4 may be overestimated as a result of the limited range of bulk density covered in the experiment with MC ($\rho_b \approx 9$ mol/L, as opposed to $\rho_b \approx 18$ mol/L for the measurements on AC). Most importantly, these estimates of ρ_{max} are systematically larger than the liquid density values at the boiling point of the adsorptive (21.1 mol/L for CO_2 at 273 K and 3.47 MPa; 26.3 mol/L for CH_4 at 111.7 K and 101.35 kPa [58]). Moreover, the larger value observed for CO_2 on AC as compared to MC may be the result of a denser packing of molecules in a micropore, as compared to a mesopore. The ability of the lattice DFT model to reveal such insights on the behaviour of the adsorbed phase, makes it a useful model to understand supercritical adsorption in porous materials.

4.5. Henry constants of porous carbons

Estimates of the Henry constants were obtained by describing the experimental data on both carbons with the Virial equation (Eq. (12)). The corresponding virial plots are presented in Fig. 7 for both (a) MC and (b) AC, where the points that have been used to obtain the Henry constant from a linear extrapolation to zero loading are clearly visible. The obtained values are plotted in Fig. 8 as a function of the reciprocal temperature and show very good fits to a linear regression (solid lines), as expected from the van't Hoff equation (Eq. (13)). We note that for this analysis we have also considered CO_2 adsorption isotherms measured on MC using the volumetric apparatus at 0 °C, 10 °C and 25 °C (shown in the inset of Fig. 7a; raw data is available in the SI) and additional literature data on AC Norit R1 Extra [67] (shown in Fig. 8). For both adsorptives, values of the Henry constants obtained for AC are about 24 times higher than estimates on MC (at equivalent temperatures), confirming the stronger affinity of the gases to the microporous AC as compared to MC. Nevertheless, a similar selectivity towards CO_2 (estimated from the ratio of the Henry constants) is observed: 1.78 ± 0.17 for MC and 1.69 ± 0.21 for AC. These values are
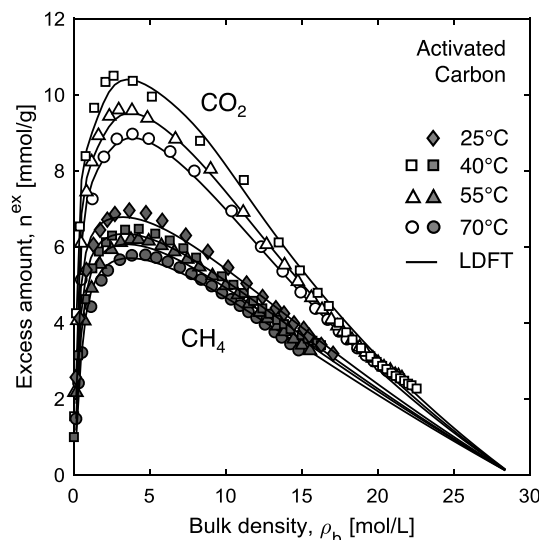

Fig. 6. Unary excess adsorption isotherms measured with CO_2 (empty symbols) and CH_4 (filled symbols) on activated carbon Norit (AC) plotted as a function of the bulk density at 25 °C, 40 °C, 55 °C and 70 °C. Details of the experimental data set are reported elsewhere [33,43]. Solid lines denote optimum fits from the lattice DFT model developed in this study (parameter values reported in Table 2).

Table 3

Parameters of the integrated van't Hoff equation, including the isosteric heat of adsorption, Δh_0 (Virial equation) and $\widetilde{\Delta h_0}$ (lattice DFT), and the corresponding pre-factors (H_0 and $\widetilde{H_0}$), for both porous carbons. The associated Henry constants are shown in Fig. 8.

Parameter	Mesoporous carbon		Activated carbon	
	CO_2	CH_4	CO_2	CH_4
	Virial equation			
H_0 (µmol g^{-1} bar^{-1})	0.0451	0.222	0.505	0.489
Δh_0 (kJ mol^{-1})	−20.8	−14.8	−22.0	−20.6
	Lattice DFT			
$\widetilde{H_0}$ (–)	2.78	2.28	6.04	5.46
$\widetilde{\Delta h_0}$ (kJ mol^{-1})	−15.3	−12.4	−13.6	−12.7

relatively low and indicate a similar affinity of CO_2 and CH_4 to the carbon surface for both materials.

The parameters obtained upon fitting the van't Hoff equation to the Henry constants are reported in Table 3 and include the isosteric heat of adsorption, Δh_0 (Virial equation fitted to experimental data) and $\widetilde{\Delta h_0}$ (lattice DFT), and the associated pre-factors (H_0 and $\widetilde{H_0}$). The isosteric heat estimated from the experiments is similar for both carbons and both adsorptives ($\Delta h_0 \approx -20$ kJ/mol), but is systematically larger than the value predicted by the lattice DFT model ($\widetilde{\Delta h_0} \approx -14$ kJ/mol). This discrepancy may be the result of a lack of experimental points at sufficiently low pressures to constrain the fitting of model. Nevertheless, these estimates are larger than the latent heat of vapourisation of the two gases (i.e. $\Delta h_{vap} = -10.3$ kJ/mol for CO_2 at 273.15 K and $\Delta h_{vap} = -8.2$ kJ/mol for CH_4 at 112 K [58]), in agreement with the expectation that for physisorption, $\Delta h_0 / \Delta h_{vap} < 1.5 - 2$ [68].

5. Discussion

One of the key features of the lattice DFT model for describing supercritical adsorption is the explicit incorporation of the textural properties of the adsorbent, including the size distribution and geometry of pores. The benefits of this are evident in the ability of this modelling approach to correctly capture the uptake of supercritical fluids on a variety of adsorbents with distinct PSD, such as the microporous and mesoporous carbon materials considered in this study.
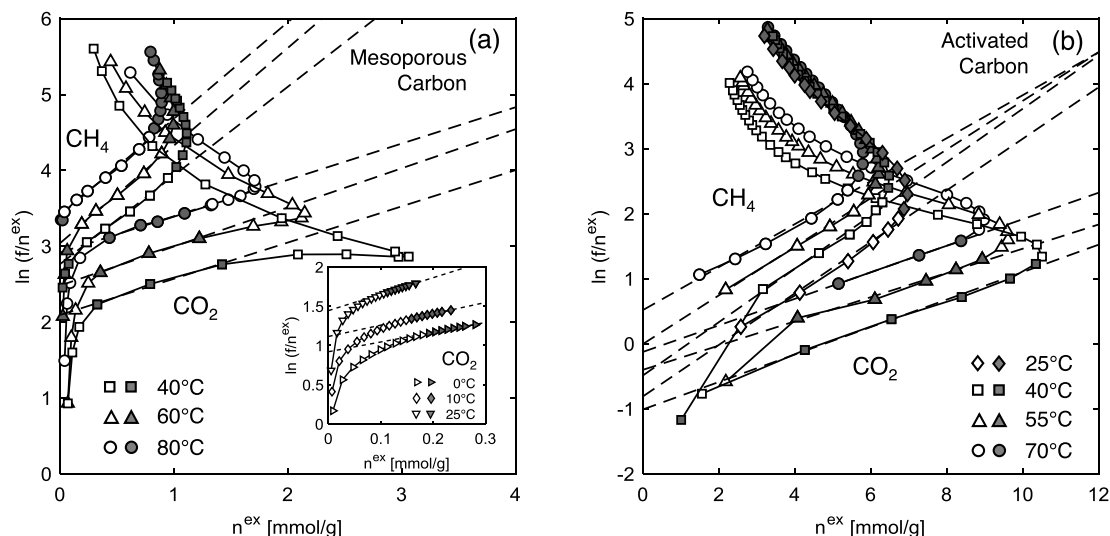
Fig. 7. The Virial plot [$\ln(f/n^{ex})$ vs. n^{ex}] for (a) MC (inset shows subcritical CO_2 data) and (b) AC. All experimental points are connected with solid lines. For CO_2, filled points represent the experimental data that were considered part of the linear region, and empty points are the residual experimental data. For the CH_4, empty points are the Virial region points and filled points are the remainder of the experimental data. The dashed lines are the linear fits at all experimental temperatures.
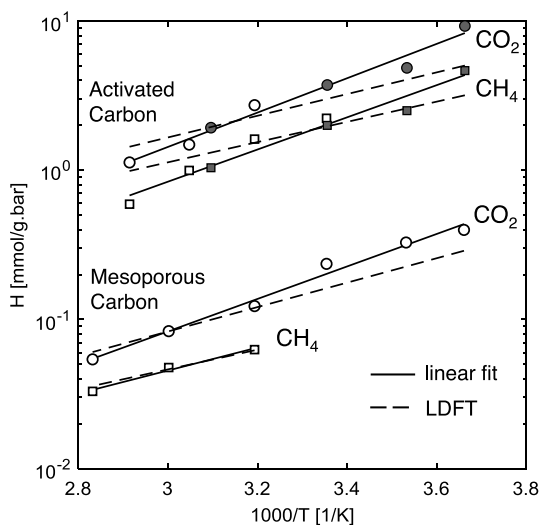

Fig. 8. Henry constants as a function of the reciprocal temperature for CO_2 and CH_4 on the two porous carbons. Data on MC have been obtained in this study. For AC, the empty symbols refer to the analysis carried out on the excess adsorption isotherms reported in [33,43], while the filled symbols are data reported in [67] on a similar AC. Solid lines denote linear fits to the experimental data, while the dashed lines represent prediction from the fitted cylindrical lattice DFT model.

The latter represents a particularly challenging material, because of the peculiar phase-behaviour of fluids within pores of diameters in the order of 10 nm, where interactions between the solid and the fluid are as important as those between the fluid molecules themselves. Once calibrated against experimental data the lattice DFT model can provide additional insights on the behaviour of the adsorbed phase within the pores, including pore-size dependent adsorption behaviour and filling capacities, as discussed in the following sections.

5.1. Effect of pore geometry on supercritical adsorption

Fig. 9 shows the pore saturation factors obtained for MC and AC as a function of the inverse reduced temperature (T_c/T). The saturation factor is an indicator of the occupancy of the total pore space by the supercritical adsorbed phase at saturation and accounts for the inefficient packing of molecules, which may depend on both the temperature and the effective size of the adsorbate molecules. Several observations can be made here; first, for a given adsorbent, CO_2 and CH_4 outline a common linear trend, suggesting that temperature is the main driver in controlling the pore filling behaviour. The fact that the saturation factor increases upon approaching the critical temperature of the fluid further indicates that near complete saturation of the pore space may be achieved at near critical conditions, in agreement with early observations of critical adsorption on graphitised carbon black [69]. Second, saturation factors obtained on MC ($c_{sat} = 0.3 - 0.8$) are systematically lower than those on AC ($c_{sat} = 0.7 - 1$) at equivalent reduced temperature. This result confirms observations from textural analysis in that micropores tend to be readily filled with an adsorbed phase, with a relatively weak dependence on the temperature. On the contrary, complete filling of mesopores can be reached only near the critical temperature of the fluid ($T_c/T > 0.95$). These observations provides additional indications of pore-size dependent adsorption behaviour and of the importance of using adsorption models that can account for it.

Also shown in Fig. 9 are the saturation factors obtained when a one-dimensional slit is used to describe the geometry of the pores in the lattice DFT model. The equations used are equivalent to those reported in an earlier publication [56] and are summarised in the SI, together with both fitted and input model parameters. For the calculations, the lattice configuration (cubic) and discretised PSD (shown in Fig. 3) were the same as those used for the cylindrical pore model. We note that the selected (physical) pore-sizes ($D_{p,J}$) differ in terms of the number of layers considered in the given geometry, as $D_{p,J} = d(2J - 1)$ for a cylinder and $D_{p,J} = Jd$ for a slit. Accordingly, for MC $J = [2, 6, 15]$ (cylinder) and $J = [3, 11, 29]$ (slit), while for AC $J = [3, 11]$ (cylinder) and $J = [5, 21]$ (slit). As it can be seen in Fig. 9, for both materials the majority of the obtained values are larger than one, indicating (i) that the slit geometry requires a larger pore volume and (ii) that the latter is greater than the total pore volume available – a physical limit – to achieve amounts adsorbed that are equivalent to the cylindrical model. As discussed below, the reason for this can be traced back to the effective interaction between the adsorbate and the adsorbent that is described by the lattice coordination number at the wall (z_J^{a+} for a cylinder and z^a for a slit). The cylindrical lattice allows for this coordination number to be larger ($z_J^{a+} > z^a = 1$) and to depend on the size of the pore (z_J^{a+} increases with decreasing J), features that are key to accurately describe supercritical adsorption in porous carbons.
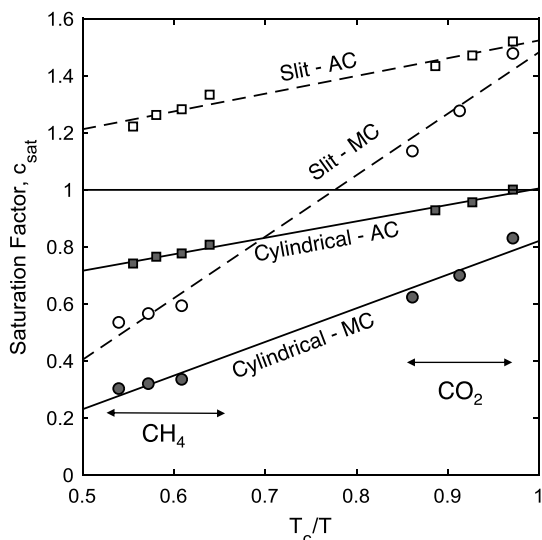
Fig. 9. The pore saturation factor, c_{sat}, as a function of T_c/T for mesoporous carbon (circles) and activated carbon (squares) obtained with the lattice DFT model that uses cylindrical (filled symbols) and slit pores (empty symbols). Linear fits for both pore geometries and materials are also shown. Note that the relevant plot for calculating Henry constants, namely $\ln(c_{sat})$ vs. T_c/T, is shown in the SI.

Fig. 10 shows the (a) CO_2 and (b) CH_4 effective surface interaction parameter ($\varepsilon_{sf} z_J^{a+}/k_B$) as a function of the number of layers J for the cylindrical and slit lattice model and for both carbon materials. For the cylindrical pore model $|\varepsilon_{sf} z_J^{a+}/k_B|$ decreases strongly with increasing pore size, while for the slit pore model its value is constant ($z_J^{a+} = z^a = 1$) and does not depend on the number of layers (shown in the plots by the dashed horizontal lines). Most significantly, for a given adsorptive the two porous carbons outline a common curve, thus supporting the robustness of the proposed approach in capturing surface–fluid interactions correctly, irrespective of the PSD. In fact, the latter manifests itself through the *average* effective interaction energy, $\overline{\varepsilon}_{sf}/k_B$, which accounts for the contribution of each pore class to the surface area of the porous carbon. Not surprisingly, the estimated values (computed with Eq. (8) and shown as horizontal solid lines) are larger (more negative) for AC as compared to MC, as a result of a larger amount of microporosity. Interestingly, these average values are comparable to those obtained with the slit model (ε_{sf}/k_B), a result that may be a mere coincidence, given that the latter produces unphysical values for the pore saturations factors ($c_{sat} > 1$). As anticipated above, the use of a cylindrical lattice does not only provide for a better representation of the true geometry of the pores in the two carbon materials, but also leads to estimated pore filling capacities that are physically more meaningful.

5.2. The use (and misuse) of the Langmuir adsorption model

The Langmuir model, Eq. (16), is often used to depict supercritical adsorption isotherms measured in microporous materials, such as activated carbon [36] and coal [70]:

$$n^{ex} = \left(\frac{n^\infty K_L f}{1 + K_L f} \right) \left(1 - \frac{\rho_b}{\rho_a} \right) \quad (16)$$

where n^∞ is the saturation limit (monolayer), K_L is the Langmuir equilibrium constant and f is the fugacity. The second term on the right-hand side of the equation is the correction required to describe excess adsorption data upon assuming a certain behaviour for the density of the adsorbed phase, ρ_a [71]. Because it qualitatively describes a Type I isotherm, the Langmuir model performs reasonably well on microporous carbons by appropriate choice of constant values for n^∞, K_L and ρ_a, although often the main assumptions of the model are relaxed (e.g., n^∞ is let to be dependent on the temperature [36,72]).

However, its suitability to describe supercritical adsorption on meso-porous materials is questionable, as suggested by the lack of application in the literature.

A comparison is presented in Fig. 11 between the application of the lattice DFT (solid lines — same as those presented in Fig. 4) and the Langmuir adsorption model (dashed lines) to describe experimental adsorption data obtained on (a) MC and (b) AC. To utilise the Langmuir model, we have assumed a constant adsorbed-phase density and set its value to be the same as ρ_{max} in the lattice DFT model (see Table 2), while fitting the parameters n^∞ and K_L (values reported in the caption of the figure). It can be seen that the Langmuir model clearly fails at describing the CO_2 isotherms measured on the two carbons. The discrepancy is larger for MC as compared to AC, as a result of the larger contribution of mesoporosity that gives rise to pore confinement effects and to the those isotherm shape features that are characteristic of mesoporous materials, i.e., a late maximum and the nonlinear behaviour at large densities. On the contrary, both models perform equally well on the data obtained using CH_4 on both porous carbons, with only slight differences appearing at large bulk densities ($\rho_b > 10$ mol/L). Well above the critical temperature or when microporosity dominates, the assumption of a constant adsorbed phase density is likely more justified and the excess adsorption isotherm beyond the maximum becomes more linear. The use of the Langmuir model (and many other "Type I" adsorption models [42]) requires explicit information on the behaviour of the adsorbed-phase density (or volume). The most commonly adopted approaches assume a constant value for this parameter, although this is very likely to be dependent on both the bulk density and PSD of the material [71]. Unless this information is obtained from an independent measurement, the application of such models to describe supercritical adsorption on mesoporous materials is inherently flawed.

6. Conclusion

We have presented an integrated experimental and modelling approach for the characterisation of porous carbons using gas adsorption data acquired at subcritical and supercritical conditions. While robust experimental protocols and theoretical frameworks exist for extracting textural information from the adsorption of N_2 and Ar at their standard boiling point, attempts of using supercritical data have so far been only partly successful, because of the following two reasons. First, the weaker sensitivity of supercritical adsorption on the geometry and size of pores requires the measurements to be conducted at sufficiently large pressures and at temperatures that are relatively close (10 K in this study) to the critical temperature of the adsorptive. Second, the simulation of supercritical adsorption has almost exclusively been done for micro- and meso-slit pores, thereby neglecting the topological characteristics of many porous carbonaceous structures.

The workflow was applied on unary adsorption isotherms measured with CO_2 and CH_4 up to 25 MPa at 40 °C, 60 °C and 80 °C on a commercial mesoporous carbon. To this end, a model based on the lattice Density Functional Theory (DFT) has been newly developed for pores of cylindrical geometry, whose characteristic sizes where identified upon calibration against outcomes from textural analysis by Ar (87 K) adsorption. It would be straightforward to extend the lattice DFT model to a hybrid formulation, where both slit and cylindrical pores are used, as it has been proposed for the textural characterisation of subcritical adsorption data measured on carbons. The general applicability of the workflow was validated by extending the analysis to a comprehensive literature data set on a microporous activated carbon. We contend that the model's predictive capability can be integral to the characterisation of other carbons at supercritical conditions. Moreover, by extending the characterisation effort over a wider range of conditions, the combination of sub- and super-critical adsorption data increases the robustness of the analysis, in addition to mimicking more closely the conditions of many industrial applications of adsorption.
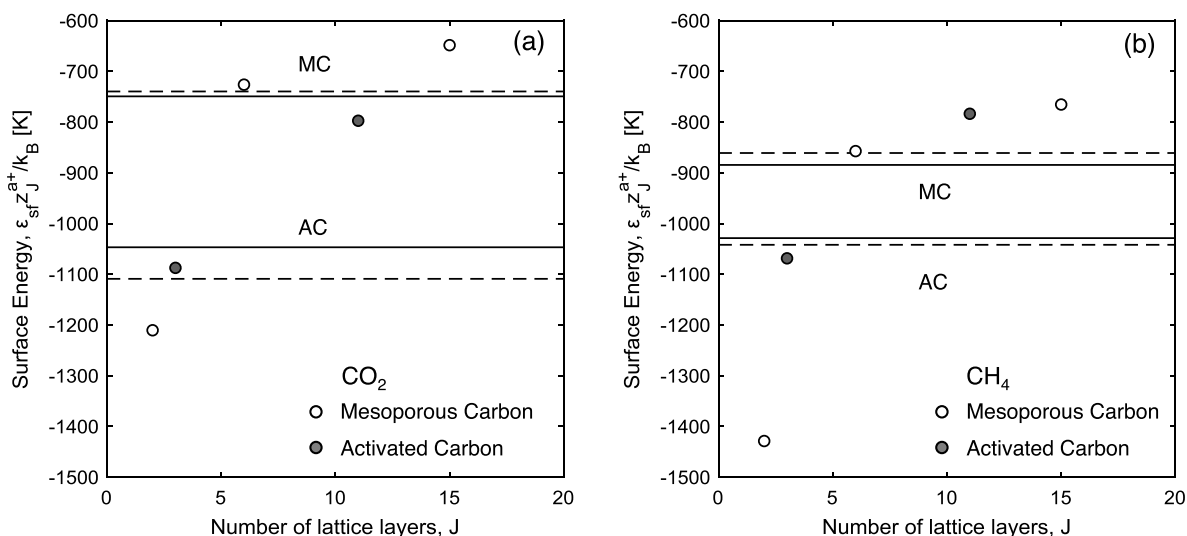
Fig. 10. (a) CO_2 and (b) CH_4 effective surface interaction parameter ($\varepsilon_{sf} z_J^{a+}/k_B$) as a function of the number of layers J for the cylindrical and slit lattice model and for both carbon materials. Symbols represent estimates for the pore classes used to describe the two adsorbents using the cylindrical lattice DFT model, while the horizontal lines represent average values for the cylindrical ($\bar{\varepsilon}_{sf}/k_B$ - solid) and slit pore model ($\bar{\varepsilon}_{sf}/k_B = \varepsilon_{sf}/k_B$ - dashed).
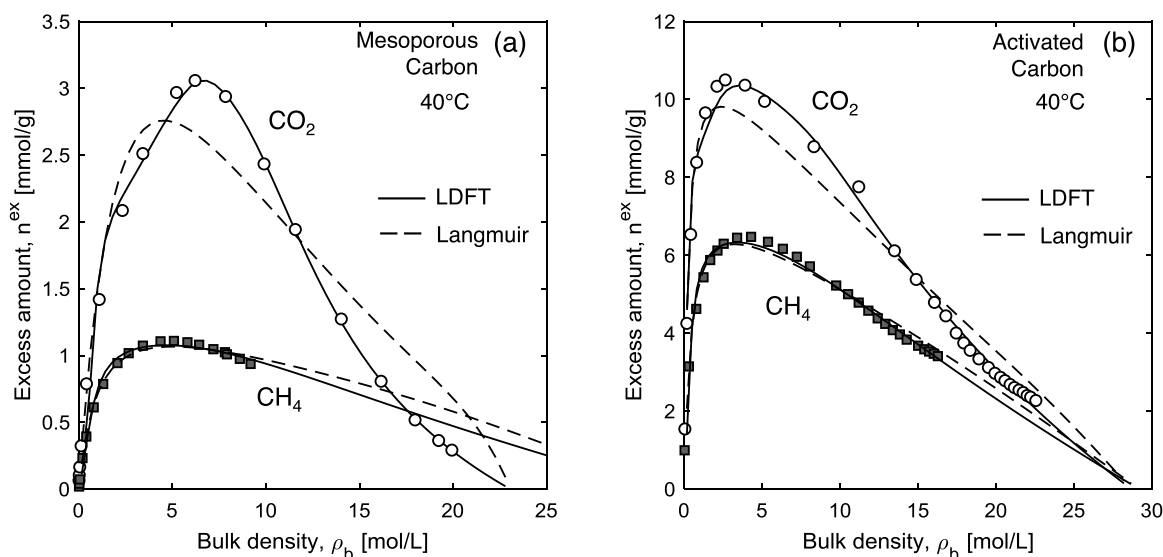

Fig. 11. A comparison between the description of CO_2 and CH_4 supercritical adsorption obtained upon application of the lattice DFT (solid lines) and Langmuir model (dashed lines, Eq. (16)) on experimental data measured on (a) mesoporous carbon and (b) activated carbon at 40 °C. The Langmuir parameters [n^∞ (mmol/g), K_L (1/bar)] are: MC — [24.50, 0.0033] (CO_2) and [1.66, 0.033] (CH_4); AC — [12.75, 0.14] (CO_2) and [8.32, 0.082] (CH_4).

CRediT authorship contribution statement

Humera Ansari: Conceptualization, Methodology, Investigation, Formal analysis, Visualization, Writing - review & editing. **Lisa Joss:** Conceptualization, Methodology, Investigation, Writing - original draft. **Junyoung Hwang:** Methodology, Investigation, Software. **J.P. Martin Trusler:** Conceptualization, Supervision, Writing - review & editing, Funding acquisition. **Geoffrey Maitland:** Conceptualization, Supervision, Writing - review & editing, Funding acquisition. **Ronny Pini:** Conceptualization, Methodology, Supervision, Visualization, Writing - review & editing, Funding acquisition.

Declaration of competing interest

The authors declare that they have no known competing financial interests or personal relationships that could have appeared to influence the work reported in this paper.

Appendix A. Supplementary data

Supplementary material related to this article can be found online at https://doi.org/10.1016/j.micromeso.2020.110537.

References

[1] A.D. Ebner, J.A. Ritter, State-of-the-art adsorption and membrane separation processes for carbon dioxide production from carbon dioxide emitting industries, Sep. Sci. Technol. 44 (6) (2009) 1273–1421.

[2] S. Sircar, T.C. Golden, M.B. Rao, Activated carbon for gas separation and storage, Carbon 34 (1) (1996) 1–12.

[3] J.P. Marco-Lozar, M. Kunowsky, F. Suárez-García, J.D. Carruthers, A. Linares-Solano, Activated carbon monoliths for gas storage at room temperature, Energy Environ. Sci. 5 (12) (2012) 9833–9842.

[4] M. Mastalerz, L. He, Y.B. Melnichenko, J.A. Ru, Porosity of coal and shale: Insights from gas adsorption and SANS/USANS techniques, Energy Fuels 26 (8) (2012) 5109–5120.

[5] M. Mazzotti, R. Pini, G. Storti, Enhanced coalbed methane recovery, J. Supercrit. Fluids 47 (3) (2009) 619–627.

[6] M. Wang, K. Huang, W. Xie, X. Dai, Current research into the use of supercritical CO2 technology in shale gas exploitation, Int. J. Mining Sci. Technol. 29 (5) (2019) 739–744.

[7] K. Kaneko, R.F. Cracknell, D. Nicholson, Nitrogen adsorption in slit pores at ambient temperatures: Comparison of simulation and experiment, Langmuir 10 (12) (1994) 4606–4609.

[8] A.V. Neimark, P.I. Ravikovitch, Calibration of pore volume in adsorption experiments and theoretical models, Langmuir 13 (19) (1997) 5148–5160.

[9] S. Jiang, J.A. Zollweg, K.E. Gubbins, High-pressure adsorption of methane and ethane in activated carbon and carbon fibers, J. Phys. Chem. 98 (22) (1994) 5709–5713.

[10] B. Yan, X. Yang, Adsorption prediction for three binary supercritical gas mixtures on activated carbon based on a NDFT/PSD aoach, Chem. Eng. Sci. 60 (12) (2005) 3267–3277.

[11] T.X. Nguyen, S.K. Bhatia, D. Nicholson, Prediction of high-pressure adsorption equilibrium of supercritical gases using density functional theory, Langmuir 21 (7) (2005) 3187–3197.

[12] H. Yi, Y. Li, X. Tang, F. Li, K. Li, Q. Yuan, X. Sun, Effect of the adsorbent pore structure on the separation of carbon dioxide and methane gas mixtures, J. Chem. Eng. Data 60 (5) (2015) 1388–1395.

[13] S. Brandani, E. Mangano, L. Sarkisov, Net, excess and absolute adsorption and adsorption of helium, Adsorption 22 (2) (2016) 261–276.

[14] D.M. Ruthven, Principles of Adsorption and Adsorption Processes, John Wiley & Sons, USA, 1984.

[15] H. Qinglin, S.M. Sundaram, S. Farooq, Revisiting transport of gases in the micropores of carbon molecular sieves, Langmuir 19 (2) (2003) 393–405.

[16] C. Liang, Z. Li, S. Dai, Mesoporous carbon materials: Synthesis and modification, Angew. Chem. Int. Ed. 47 (20) (2008) 3696–3717.

[17] K.A. Cychosz, R. Guillet-Nicolas, J. García-Martínez, M. Thommes, Recent advances in the textural characterization of hierarchically structured nanoporous materials, Chem. Soc. Rev. 46 (2) (2017) 389–414.

[18] P.A. Monson, Understanding adsorption/desorption hysteresis for fluids in mesoporous materials using simple molecular models and classical density functional theory, Microporous Mesoporous Mater. 160 (2012) 47–66.

[19] J. Specovius, G.H. Findenegg, Study of a fluid/solid interface over a wide density range including the critical region. i. surface excess of ethylene/graphite, Ber. Bunsenges. Phys. Chem. 84 (7) (1980) 690–696.

[20] M. Thommes, G.H. Findenegg, Pore condensation and critical-point shift of a fluid in controlled-pore glass, Langmuir 10 (11) (1994) 4270–4277.

[21] M. Thommes, J. Morell, K.A. Cychosz, M. Fröba, Combining nitrogen, argon, and water adsorption for advanced characterization of ordered mesoporous carbons (CMKs) and periodic mesoporous organosilicas (PMOs), Langmuir 29 (48) (2013) 14893–14902.

[22] M. Thommes, K. Kaneko, A.V. Neimark, J.P. Olivier, F. Rodriguez-Reinoso, J. Rouquerol, K.S.W. Sing, Physisorption of gases, with special reference to the evaluation of surface area and pore size distribution (IUPAC technical report), Pure Aied Chem. 87 (9–10) (2015) 1051.

[23] K.A. Sosin, D.F. Quinn, Using the high pressure methane isotherm for determination of pore size distribution of carbon adsorbents, J. Porous Mater. 1 (1) (1995) 111–119.

[24] V.Y. Gusev, J.A. O'Brien, N.A. Seaton, A self-consistent method for characterization of activated carbons using supercritical adsorption and Grand canonical Monte Carlo simulations, Langmuir 13 (10) (1997) 2815–2821.

[25] T. Suzuki, R. Kobori, K. Kaneko, Grand canonical Monte Carlo simulation-assisted pore-width determination of molecular sieve carbons by use of ambient temperature N2 adsorption, Carbon 38 (2000) 630–633.

[26] T. Hocker, A. Rajendran, M. Mazzotti, Measuring and modeling supercritical adsorption in porous solids. carbon dioxide on 13X zeolite and on silica gel, Langmuir 19 (4) (2003) 1254–1267.

[27] L. Zhou, S. Bai, W. Su, J. Yang, Y. Zhou, Comparative study of the excess versus absolute adsorption of CO2 on superactivated carbon for the near-critical region, Langmuir 19 (7) (2003) 2683–2690.

[28] E.A. Ustinov, D.D. Do, High-pressure adsorption of supercritical gases on activated carbons: an improved approach based on the density functional theory and the bender equation of state, Langmuir 19 (20) (2003) 8349–8357.

[29] Y. Liu, J. Wilcox, Molecular simulation of CO2 adsorption in micro- and mesoporous carbons with surface heterogeneity, Int. J. Coal Geol. 104 (2012) 83–95.

[30] P. Malbrunot, D. Vidal, J. Vermesse, R. Chahine, T.K. Bose, Adsorption measurements of argon, neon, krypton, nitrogen, and methane on activated carbon up to 650 MPa, Langmuir 8 (2) (1992) 577–580.

[31] J.H. Chen, D.S.H. Wong, C.S. Tan, R. Subramanian, C.T. Lira, M. Orth, Adsorption and desorption of carbon dioxide onto and from activated carbon at high pressures, Ind. Eng. Chem. Res. 36 (7) (1997) 2808–2815.

[32] R. Humayun, D.L. Tomasko, High-resolution adsorption isotherms of supercritical carbon dioxide on activated carbon, AIChE J. 46 (10) (2000) 2065–2075.

[33] A. Herbst, P. Harting, Thermodynamic description of excess isotherms in high-pressure adsorption of methane, argon and nitrogen, Adsorption 8 (2) (2002) 111–123.

[34] M. Sudibandriyo, Z. Pan, J.E. Fitzgerald, R.L. Robinson, K.A.M. Gasem, Adsorption of methane, nitrogen, carbon dioxide, and their binary mixtures on dry activated carbon at 318.2 K and pressures up to 13.6 MPa, Langmuir 19 (13) (2003) 5323–5331.

[35] R. Pini, S. Ottiger, A. Rajendran, G. Storti, M. Mazzotti, Reliable measurement of near-critical adsorption by gravimetric method, Adsorption 12 (5) (2006) 393–403.

[36] J. Schell, N. Casas, R. Pini, M. Mazzotti, Pure and binary adsorption of CO2, H2, and N2 on activated carbon, Adsorption 18 (1) (2012) 49–65.

[37] G. Rother, E.G. Krukowski, D. Wallacher, N. Grimm, R.J. Bodnar, D.R. Cole, Pore size effects on the sorption of supercritical CO2 in mesoporous CPG-10 silica, J. Phys. Chem. C 116 (1) (2012) 917–922.

[38] O.D. Giovanni, W. Dörfler, M. Mazzotti, M. Morbidelli, Adsorption of supercritical carbon dioxide on silica, Langmuir 17 (14) (2001) 4316–4321.

[39] N. Tatsuda, Y. Goto, N. Setoyama, Y. Fukushima, Adsorption of carbon dioxide on mesoporous silicas near the critical temperature, Adsorption Sci. Technol. 23 (9) (2005) 763–776.

[40] M.S. Gruszkiewicz, G. Rother, D.J. Wesolowski, D.R. Cole, D. Wallacher, Direct measurements of pore fluid density by vibrating tube densimetry, Langmuir 28 (11) (2012) 5070–5078.

[41] R. Pini, Interpretation of net and excess adsorption isotherms in microporous adsorbents, Microporous Mesoporous Mater. 187 (2014) 40–52.

[42] D.D. Do, H.D. Do, Adsorption of supercritical fluids in non-porous and porous carbons: analysis of adsorbed phase volume and density, Carbon 41 (9) (2003) 1777–1791.

[43] E.A. Ustinov, D.D. Do, A. Herbst, R. Staudt, P. Harting, Modeling of gas adsorption equilibrium over a wide range of pressure: A thermodynamic aoach based on equation of state, J. Colloid Interface Sci. 250 (1) (2002) 49–62.

[44] P. Malbrunot, D. Vidal, J. Vermesse, R. Chahine, T.K. Bose, Adsorbent helium density measurement and its effect on adsorption isotherms at high pressure, Langmuir 13 (3) (1997) 539–544.

[45] CRC Handbook of Chemistry and Physics, eighty-seventh ed., CRC Press, Taylor & Francis Group, Boca Raton, FL, 2006.

[46] C. Weinberger, S. Vetter, M. Tiemann, T. Wagner, Assessment of the density of (meso)porous materials from standard volumetric physisorption data, Microporous Mesoporous Mater. 223 (2016) 53–57.

[47] R. Span, W. Wagner, A new equation of state for carbon dioxide covering the fluid region from the triplepoint temperature to 1100 K at pressures up to 800 MPa, J. Phys. Chem. Ref. Data 25 (6) (1996) 1509–1596.

[48] U. Setzmann, W. Wagner, A new equation of state and tables of thermodynamic properties for methane covering the range from the melting line to 625 K at pressures up to 100 MPa, J. Phys. Chem. Ref. Data 20 (6) (1991) 1061–1155.

[49] F. Dreisbach, H.W. Lösch, Magnetic suspension balance for simultaneous measurement of a sample and the density of the measuring fluid, J. Therm. Anal. Calorim. 62 (2) (2000) 515–521.

[50] X. Yang, R. Kleinrahm, M.O. McLinden, M. Richter, Uncertainty analysis of adsorption measurements using commercial gravimetric sorption analyzers with simultaneous density measurement based on a magnetic-suspension balance, Adsorption 26 (4) (2020) 645–659.

[51] S. Ono, S. Kondo, Molecular theory of surface tension in liquids, Struct. Liq. Encyclopedia Phys. 3–10 (1960) 134–280.

[52] G.L. Aranovich, M.D. Donohue, A new model for lattice systems, J. Chem. Phys. 105 (16) (1996) 7059–7063.

[53] G. Aranovich, M. Donohue, Analysis of adsorption isotherms: Lattice theory predictions, classification of isotherms for gas-solid equilibria, and similarities in gas and liquid adsorption behavior, J. Colloid Interface Sci. 200 (2) (1998) 273–290.

[54] S. Ottiger, R. Pini, G. Storti, M. Mazzotti, Measuring and modeling the competitive adsorption of CO2, CH4, and N2 on a dry coal, Langmuir 24 (17) (2008) 9531–9540.

[55] M. Sudibandriyo, S.A. Mohammad, R.L. Robinson Jr., K.A.M. Gasem, Ono-Kondo lattice model for high-pressure adsorption: Pure gases, Fluid Phase Equilib. 299 (2) (2010) 238–251.

[56] J. Hwang, L. Joss, R. Pini, Measuring and modelling supercritical adsorption of CO2 and CH4 on montmorillonite source clay, Microporous Mesoporous Mater. 273 (2019) 107–121.

[57] A. Qajar, H. Daigle, M. Prodanović, The effects of pore geometry on adsorption equilibrium in shale formations and coal-beds: Lattice density functional theory study, Fuel 163 (2016) 205–213.

[58] P.J. Linstrom, W.G. Mallard, NIST Chemistry WebBook, NIST Standard Reference Database Number 69, Gaithersburg MD, 20899: National Institute of Standards and Technology.

[59] Sigma-Aldrich, Carbon, mesoporous, 2017.

[60] A.B. Fuertes, G. Marbán, D.M. Nevskaia, Adsorption of volatile organic compounds by means of activated carbon fibre-based monoliths, Carbon 41 (1) (2003) 87–96.

[61] D. Hulicova-Jurcakova, A.M. Puziy, O.I. Poddubnaya, F. Suárez-García, J.M.D. Tascón, G.Q. Lu, Highly stable performance of supercapacitors from phosphorus-enriched carbons, J. Am. Chem. Soc. 131 (14) (2009) 5026–5027.

[62] T.E. Rufford, G.C.Y. Watson, T.L. Saleman, P.S. Hofman, N.K. Jensen, E.F. May, Adsorption equilibria and kinetics of methane + nitrogen mixtures on the activated carbon Norit RB3, Ind. Eng. Chem. Res. 52 (39) (2013) 14270–14281.

[63] J.-P. Bellat, I. Bezverkhyy, G. Weber, S. Royer, R. Averlant, J.-M. Giraudon, J.-F. Lamonier, Capture of formaldehyde by adsorption on nanoporous materials, J. Hard Mater. 300 (2015) 711–717.

[64] H. Aljamaan, R. Holmes, V. Vishal, R. Haghpanah, J. Wilcox, A.R. Kovscek, CO2 storage and flow capacity measurements on idealized shales from dynamic breakthrough experiments, Energy Fuels (2017).

[65] J. Moellmer, E.B. Celer, R. Luebke, A.J. Cairns, R. Staudt, M. Eddaoudi, M. Thommes, Insights on adsorption characterization of metal–organic frameworks: A benchmark study on the novel *soc*-MOF, Microporous Mesoporous Mater. 129 (3) (2010) 345–353.

[66] E.W. Lemmon, I. Bell, M.L. Huber, M.O. McLinden, NIST Standard Reference Database 23: Reference Fluid Thermodynamic and Transport Properties-REFPROP, Version 10.0, National Institute of Standards and Technology, 2018.

[67] S. Himeno, T. Komatsu, S. Fujita, High-pressure adsorption equilibria of methane and carbon dioxide on several activated carbons, J. Chem. Eng. Data 50 (2) (2005) 369–376.

[68] D.M. Ruthven, Adsorption, fourth ed., in: Kirk-Othmer Encyclopedia of Chemical Technology, vol. 1, Wiley-Interscience, New York, 1991.

[69] S. Blümel, G.H. Findenegg, Critical adsorption of a pure fluid on a graphite substrate, Phys. Rev. Lett. 54 (5) (1985) 447–450.

[70] R. Pini, S. Ottiger, L. Burlini, G. Storti, M. Mazzotti, Role of adsorption and swelling on the dynamics of gas injection in coal, J. Geophys. Res. 114 (B4) (2009).

[71] K. Murata, M. El-Merraoui, K. Kaneko, A new determination method of absolute adsorption isotherm of supercritical gases under high pressure with a special relevance to density-functional theory study, J. Chem. Phys. 114 (9) (2001) 4196–4205.

[72] R. Pini, S. Ottiger, L. Burlini, G. Storti, M. Mazzotti, Sorption of carbon dioxide, methane and nitrogen in dry coals at high pressure and moderate temperature, Int. J. Greenh. Gas Control 4 (1) (2010) 90–101.